

Plasma instability of magnetically enhanced vacuum arc thruster

L. Chang,^{1, a)} T. P. Zhang,² X. Y. Hu,¹ X. M. Wu,² and X. F. Sun²

¹⁾*School of Aeronautics and Astronautics, Sichuan University, Chengdu 610065, China*

²⁾*National Key Laboratory of Science and Technology on Vacuum Technology and Physics, Lanzhou Institute of Physics, Lanzhou 730000, China*

(Dated: 30 November 2018)

A two-fluid flowing plasma model is applied to describe the plasma rotation and resulted instability evolution in magnetically enhanced vacuum arc thruster (MEVAT). Typical experimental parameters are employed, including plasma density, equilibrium magnetic field, ion and electron temperatures, cathode materials, axial streaming velocity, and azimuthal rotation frequency. It is found that the growth rate of plasma instability increases with growing rotation frequency and field strength, and with descending electron temperature and atomic weight, for which the underlying physics are explained. The radial structure of density fluctuation is compared with that of equilibrium density gradient, and the radial locations of their peak magnitudes are very close, showing an evidence of resistive drift mode driven by density gradient. Temporal evolution of perturbed mass flow in the cross section of plasma column is also presented, which behaves in form of clockwise rotation (direction of electron diamagnetic drift) at edge and anti-clockwise rotation (direction of ion diamagnetic drift) in the core, separated by a mode transition layer from $n = 0$ to $n = 1$. This work, to our best knowledge, is the first treatment of plasma instability caused by rotation and axial flow in MEVAT, and is also of great practical interest for other electric thrusters where rotating plasma is concerned for long-time stable operation and propulsion efficiency optimization.

PACS numbers: 52.35.Kt, 52.75.Di, 52.30.Ex, 52.25.Xz, 52.25.Gj

Keywords: Plasma instability, flow and rotation, vacuum arc thruster, magnetic field, two-fluid model

I. INTRODUCTION

Plasma propulsion is generally caused by jetting plasma in the opposite direction, according to Newton's third law, and accelerated either by electric force or magnetic force or both of them.¹⁻⁶ External magnetic field is usually employed for efficient plasma generation and propulsion enhancement and control.⁷⁻¹² Due to the nonuniform configurations of equilibrium magnetic field, discharge area and plume, plasma rotation driven by Lorentz force commonly occurs in various electric thrusters.¹³⁻¹⁶ A few analytical models have been developed or/and applied to describe this flowing phenomenon,¹⁷⁻²¹ but little attention was given to the resulted plasma instability which, however, can effect the propulsion efficiency, precise control, durable reliability and life time significantly.^{22,23} This paper considers an emerging plasma propulsion technology, namely magnetically enhanced vacuum

^{a)}Electronic mail: leichang@scu.edu.cn

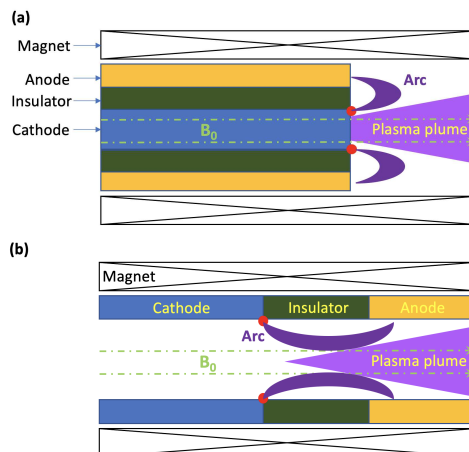


FIG. 1. Schematics of typical magnetically enhanced vacuum arc thruster (MEVAT): (a) coaxial-type, (b) ring-type.

arc thruster (MEVAT),^{24–28} as an example and studies the instability evolution caused by plasma rotation and axial flow in detail. Schematics of the typical coaxial-type and ring-type MEVATs are shown in Fig. 1, which illustrate the radial expansion of plasma plume across the confining field lines, leading to azimuthal rotation. Axial equilibrium field is usually employed to reduce the divergence of plasma plume and thereby increasing the propulsion efficiency, which is relatively low for unmagnetized vacuum arc thrusters, making the MEVAT a promising candidate to provide micro propulsion for small spacecrafts.²⁸ The findings achieved here are also applicable to other types of electric thrusters with the involvement of external magnetic field, as long as the plasma rotation and flow are concerned for stable, efficient and safe operation.

Specifically, a two-fluid flowing plasma model developed originally for interpreting wave oscillations in vacuum arc centrifuge,²⁹ which is a cylindrical, rapidly rotating, low temperature, and confined plasma column,¹⁸ will be employed, together with a shooting numerical scheme for finding solutions. It will show that the instability strength peaks near the maximum of equilibrium density gradient, an evidence of resistive drift mode, and it becomes larger for higher rotation frequency, higher field strength, lower electron temperature and lower atomic weight. Temporal evolutions of perturbed mass flow in cross section will be also shown. The paper is organized as follows: Sec. II describes the theoretical model and steady-state and perturbed solutions, Sec. III presents the employed numerical scheme, dispersion relation, fluctuation structure and parameter dependence, and Sec. IV summarizes the whole paper and remarks the possible applications of this work to other electric thrusters.

II. TWO-FLUID FLOWING PLASMA MODEL

A. Model assumptions

The employed two-fluid flowing plasma model is based on the following assumptions:

1. Ions of different charge can be treated as a single species with average charge Z .

2. Plasma is quasi-neutral so that $n_e = Zn_i$.
3. Steady-state plasma is azimuthally symmetric and has no axial structure.
4. The effects of plasma fluctuation on external magnetic field is negligible.
5. Finite Larmor radius and viscosity effects are not considered.
6. Electron inertia can be neglected for the range of frequency considered.
7. Ion and electron temperatures (T_i and T_e) are uniform across the plasma column.
8. Steady-state ion density distribution is in form of $n_0 = n_{i0} \exp[-(r/R)^2]$, with n_{i0} the on-axis ion density and R the characteristic radius where the density is $1/e$ of its on-axis value.
9. Steady-state velocities of ions and electrons are in forms of $\mathbf{v}_i = (0, \omega_i r, v_{iz})$ and $\mathbf{v}_e = [0, \omega_e(r)r, v_{ez}(r)]$, respectively, with ω_i the ion rigid rotor rotation frequency, v_{iz} the ion uniform axial streaming velocity, $\omega_e(r)$ the electron rotation frequency, and $v_{ez}(r)$ the electron streaming velocity.
10. Radial diffusion of both ions and electrons caused by electron-ion collision can be neglected.

Moreover, length and time are normalized to R and $1/\omega_{ic}$ respectively, with $\omega_{ic} = ZeB_z/m_i$ the ion cyclotron frequency, so that a normalized cylindrical coordinate system becomes $(x, \theta, \varsigma) = (r/R, \theta, z/R)$ and $\tau = \omega_{ic}t$, with x and ς the normalized radial and axial positions, respectively.

B. Governing equations

The model consists of the momentum and continuity equations for ion and electron fluids:

$$\frac{\partial \mathbf{u}_i}{\partial \tau} + (\mathbf{u}_i \cdot \nabla) \mathbf{u}_i = -\psi(Z\nabla\chi + \lambda\nabla l_i) + \mathbf{u}_i \times \hat{\varsigma} + \delta n_s \tilde{\xi} \cdot (\mathbf{u}_e - \mathbf{u}_i), \quad (1)$$

$$\psi Z(-\nabla l_i + \nabla\chi) - \mathbf{u}_e \times \hat{\varsigma} + \delta n_s \tilde{\xi} \cdot (\mathbf{u}_i - \mathbf{u}_e) = 0, \quad (2)$$

$$-\frac{\partial l_i}{\partial \tau} = \nabla \cdot \mathbf{u}_i + \mathbf{u}_i \cdot \nabla l_i, \quad (3)$$

$$-\frac{\partial l_e}{\partial \tau} = \nabla \cdot \mathbf{u}_e + \mathbf{u}_e \cdot \nabla l_i, \quad (4)$$

with terms defined as:

$$\mathbf{u}_i = \frac{\mathbf{v}_i}{\omega_{ic}R} = (x\varphi_i, x\Omega_i, u_{i\varsigma}), \quad \mathbf{u}_e = \frac{\mathbf{v}_e}{\omega_{ic}R} = (x\varphi_e, x\Omega_e, u_{e\varsigma}),$$

$$\lambda = \frac{T_i}{T_e}, \quad \psi = \frac{k_B T_e}{m_i \omega_{ic}^2 R^2}, \quad \chi = \frac{e\phi}{k_B T_e}, \quad \tilde{\xi} = \text{diag}(\xi_\perp, \xi_\perp, 1),$$

$$l_i = \ln \frac{n_i}{n_{i0}}, n_s = \frac{\nu_{ei}}{\nu_{ei0}}, \delta = \frac{eZn_{i0}}{B_z} \frac{\eta_L}{\gamma_E}.$$

The subscript i and e refer to ion and electron parameters respectively, φ represents the normalized radial velocity divided by x , Ω stands for the normalized rotation frequency, u_ζ shows the normalized axial velocity, λ labels the ratio between ion and electron temperatures, ψ behaves a convenient constant which for $\lambda = 1$ becomes the square of the normalized ion thermal velocity, χ gives a normalized electric potential ϕ , l_i expresses the logarithm of the ratio of ion density n_i to its on-axis value n_{i0} , and n_s means the ratio of electron-ion collision frequency ν_{ei} to its on-axis value ν_{ei0} . Moreover, δ phrases the normalized resistivity parallel to external magnetic field, with η_L the electrical resistivity of Lorentz gas and γ_E the ratio of the conductivity of charge state Z to that in Lorentz gas.³⁰

C. Steady-state solution

For constant magnetic field of $\mathbf{B} = (0, 0, B_z)$, the steady-state solution is

$$\chi_0(x) = \chi_c + \left[\frac{\Omega_{i0}}{2\psi Z} (1 + \Omega_{i0}) + \frac{\lambda}{Z} \right] x^2, \quad (5)$$

with

$$\Omega_{e0} = \Omega_{i0} (1 + \Omega_{i0}) + 2\psi(\lambda + Z). \quad (6)$$

Here, χ_c is an arbitrary reference potential. Because the axial current in this model is unconstrained, which is consistent with MEVAT boundary conditions, it can be arbitrarily set to zero ($u_{i\zeta 0} = u_{e\zeta 0}$).

D. Perturbed solution

To solve the perturbed solution, a linear perturbation treatment with plasma parameters ζ is considered, namely

$$\zeta(\tau, x, \theta, \varsigma) = \zeta_0(x) + \varepsilon \zeta_1(x) e^{i(m\theta + k_\zeta \varsigma - \omega\tau)}. \quad (7)$$

Here, ε is the perturbation parameter, m is the azimuthal mode number, k_ζ is the axial wave number and ω is the angular frequency. To first order of ε , Eqs. (1)-(4) can be reduced to

$$\begin{pmatrix} \psi(l'_{i1}(y) - X'_1(y)) \\ y\varphi'_{i1}(y) \\ y\varphi'_{e1}(y) - im\Psi X'_1(y) \\ \Psi\delta\xi_\perp e^{-y} X'_1(y) \\ 0 \end{pmatrix} = \tilde{\mathbf{A}} \begin{pmatrix} l_{i1}(y) \\ X_1(y) \\ \varphi_{i1}(y) \\ \varphi_{e1}(y) \\ u_{e\zeta}(y) \end{pmatrix} \quad (8)$$

with $\tilde{\mathbf{A}}$ the matrix

$$\tilde{\mathbf{A}} = \begin{pmatrix} \frac{m\Psi C}{2\varpi y} & 0 & \frac{i\varpi}{2} - \frac{iC^2}{2\varpi} & \frac{iC}{2\varpi} & 0 \\ \frac{i}{2}(\varpi - \frac{\Psi}{\varpi}(m^2 + k_\zeta^2)) & 0 & -1 + y - \frac{mC}{2\varpi} & \frac{m}{2\varpi} & 0 \\ \frac{i}{2}(\varpi - m\Omega_{i0}^2 - 2m\Psi) & 0 & 0 & -1 + y & -\frac{ik_\zeta}{2} \\ 0 & \frac{im\Psi}{2y} & 0 & -\frac{1}{2} & 0 \\ 0 & -ik_\zeta\Psi & 0 & 0 & 0 \end{pmatrix} + \delta \begin{pmatrix} 0 & 0 & -\frac{\xi_\perp e^{-y}}{2} & \frac{\xi_\perp e^{-y}}{2} & 0 \\ 0 & 0 & 0 & 0 & 0 \\ 0 & 0 & -\frac{im\xi_\perp e^{-y}}{2} & \frac{im\xi_\perp e^{-y}}{2} & 0 \\ \xi_\perp e^{-y}(-\frac{m\Psi}{2\varpi y} + \frac{\Omega_{i0}^2}{2} + \Psi) & 0 & \frac{iC\xi_\perp e^{-y}}{2\varpi} & -\frac{i\xi_\perp e^{-y}}{2\varpi} & 0 \\ \frac{e^{-y}k_\zeta\Psi}{\varpi} & 0 & 0 & 0 & -e^{-y} \end{pmatrix}. \quad (9)$$

Here, $\varpi = \omega - m\Omega_{i0} - k_\zeta u_{\zeta 0}$ is the frequency in the frame of ion fluid, $C = 1 + 2\Omega_{i0}$, $\Psi = (\lambda + Z)\psi$, $y = x^2$ and a new dependent variable $X_1(y)$ has been introduced

$$X_1(y) = \frac{Z}{Z + \lambda}[l_{i1}(y) - \chi_1(y)]. \quad (10)$$

For large axial wavelength modes of the resistive plasma column, i. e. $k_\zeta^2 \leq \delta$, Eq. (8) turns out to be a second order differential equation

$$\left(\frac{\varpi^2 - C^2}{\varpi\Psi}\right)L(N_c)[g_1(y)] = 0, \quad (11)$$

where

$$L(N_c) = y\frac{\partial^2}{\partial y^2} + (1 - y)\frac{\partial}{\partial y} + \left(\frac{N_c}{2} - \frac{m^2}{4y}\right),$$

$$N_c = \frac{(\varpi^2 - C^2)(m + \frac{i}{2}f(y))}{\varpi - m\Omega_{i0}^2 + i\Psi f(y)} + \frac{mC}{\varpi},$$

and $f(y) = F^2 e^y$ with the normalized axial wave number $F = k_\zeta/\sqrt{\delta}$. For odd m modes, the boundary conditions are $g_1(0) = 0$ and $g_1(Y) = 0$ with the infinite radius Y representing the edge of plasma column. For even m , these conditions become $g_1'(0) = 0$ and $g_1(Y) = 0$. We only consider unstable solutions for which $\varpi^i > 0$. The solutions $\varpi = \pm C$ are stable and thereby discarded.

III. COMPUTED WAVE PHYSICS ANALYSIS

A. Numerical scheme and conditions

To solve Eq. (11) numerically for perturbed solutions, we make use of a shooting method, as did by Hole et al.²⁹ For $m = 1$ mode, the boundary conditions are $g_1(0) = g_1(Y) = 0$. The gradient at edge $g_1'(Y)$ is arbitrary because the differential equation is homogeneous. As a result, we set $g_1'(Y) = 1$. For given F , a trial ϖ is first chosen and then the solution is matched from edge to core. We adjust the complex frequency ϖ until the on-axis boundary condition is satisfied. The procedure starts from $F = 0$, for which an analytical solution for ϖ can be found from

$$N_c = \frac{m(\varpi^2 - C^2)}{\varpi - m\Omega_{i0}^2} + \frac{mC}{\varpi} = 2n + |m| \quad (12)$$

TABLE I. Typical parameters of MEVAT and PCEN (plasma centrifuge).

Parameter	MEVAT ^{20,21,28,29,31-34}	PCEN ^{29,31}
n_{i0} (on axis)	$5 \times 10^{19} \text{ m}^{-3}$	$5.2 \times 10^{19} \text{ m}^{-3}$
T_e	100 eV	2.9 eV
T_i	50 eV	2.9 eV
m_i	47.87 amu (Ti)	24.31 amu (Mg)
B_z	0.1 T	0.05 T
Z	2.0	1.5
V_{z0}	$1.3 \times 10^4 \text{ m s}^{-1}$	10^4 m s^{-1}
ω_0	201 krad s^{-1}	184 krad s^{-1}
$\omega_{ic} = \frac{B_z e Z}{m_i}$	402 krad s^{-1}	295 krad s^{-1}
$\Omega_{i0} = \frac{\omega_0}{\omega_{ic}}$	0.5	0.59
$\Psi = \left(\frac{T_i}{T_e} + Z\right) \frac{k_B T_e}{m_i \omega_{ic}^2 R^2}$	3.46	1.6
$\delta = \frac{e Z n_{i0}}{B_z} \frac{\eta L}{\gamma_E}$	7.8×10^{-5}	0.03
R (characteristic radius)	3 cm	1.43 cm

with n the number of radial nodes in the plasma column. This numerical scheme has been benchmarked by previous studies.^{18,29}

For the computational parameters, we refer to existing devices and choose published experimental data. Table I shows the typical parameters of MEVAT employed for the present computation, together with those of a plasma centrifuge (PCEN^{29,31}) for comparison. Although MEVAT has much higher electron and ion temperatures and lower rotation rate, the two-fluid model originally developed for PCEN can still well describe the flowing plasma in MEVAT. The plasma density of $n_{i0} = 5 \times 10^{19} \text{ m}^{-3}$ is close to the measurement by Keidar et al.³² Trial electron and ion temperatures are 100 eV and 50 eV, respectively, for current in order of 1 kA³³ and with reference to a previous experiment.³² The strength of external magnetic field $B_z = 0.1 \text{ T}$ is typical for various MEVATs.^{21,28} The axial stream velocity of ion fluid is set to $1.3 \times 10^4 \text{ m s}^{-1}$ according to the experiment using titanium (Ti) cathode,³⁴ which lies inside the typical range of ion velocity $10 - 50 \text{ km s}^{-1}$,³⁵⁻³⁹ and meanwhile the ion species of Ti is chosen. The rotation frequency is assumed to be half the ion cyclotron frequency, which is close to that of plasma centrifuge^{29,31} to see the effect of rotation on instability evolution more clearly, and rigid rotation is a reasonable assumption according to various jetting plasma devices.^{18,31,40} Moreover, charge number of $Z = 2$ is considered throughout the paper as a common value for different cathode materials chosen here (see Sec. IIID), and characteristic radius of $R = 0.03 \text{ m}$ is made use of referring to previous studies.^{20,28} The radial density profile is shown in Fig. 2, a typical plasma distribution near the exit of MEVAT.^{27,28} We shall compute the dispersion relation and instability physics based on these experimental data in the following sections.

B. Dispersion relation

Before presenting the obtained dispersion curve, we should check the eigenfunction associated with the computation. A typical radial variation of solved eigenfunction for $F = 0$ is shown in Fig. 3, which clearly satisfies the boundary conditions of $g_1(0) = g_1(Y) = 0$ for $m = 1$ mode. Moreover, it shows a radial mode of $n = 1$ with visible node located near $y = 2$. The computed dispersion curves in the range of $F = 0 - 1$ are illustrated in Fig. 4, compared with those for PCEN. It can be seen that the normalized growth rate of

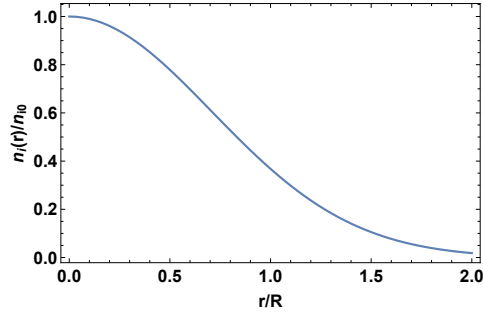


FIG. 2. Typical radial profile of plasma density near the exit of MEVAT.^{27,28}

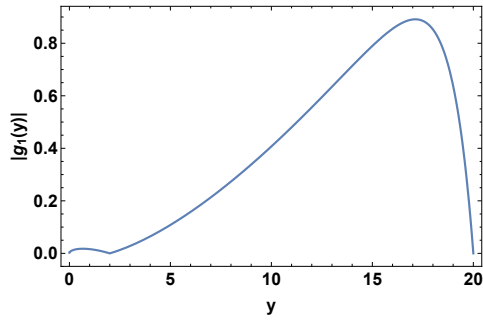


FIG. 3. Radial variation of solved eigenfunction for $F = 0$.

MEVAT peaks on axis and decreases monotonously with F , whereas the normalized growth rate of PCEN peaks off axis ($F = 0.3$) and exhibits a mode crossing near $F = 0.55$, which is caused by centrifugal instability. Relatively, the instability level (proportional to growth rate) is much more lower on MEVAT than that on PCEN for $F > 0.3$, due to significantly smaller resistivity along the external magnetic field (it will show later that the instability is a resistive drift mode). Further, the peak growth rate of $\varpi_{\max}^i = 0.324$ corresponds to $\varpi^r = -0.205$ for MEVAT, implying that the instability frequency is smaller than the sum of plasma rotation frequency and axial velocity, because $\varpi = \omega - m\Omega_{i0} - k_\zeta u_{\zeta 0}$ is the frequency in the frame of ion fluid, and it propagates in the $-\theta$ direction (same to the direction of ion diamagnetic drift); whereas, the peak growth rate of $\varpi_{\max}^i = 0.39$ corresponds to $\varpi^r = -0.007$ for PCEN, stating that the instability is near stationary in the frame of ion fluid. Overall, the normalized frequency is lower on MEVAT for $F > 0.4$, which may be attributed to lower rotation frequency and ion temperature as revealed in a previous study.¹⁸

C. Fluctuation structure

To show a cross sectional view of the mode structure, the vector field of linearly perturbed mass flow was calculated through $m_i(n_{i1}\mathbf{u}_{i0} + n_{i0}\mathbf{u}_{i1})$. We computed the perturbed velocity components $\mathbf{u}_{i1} = (x\varphi_{i1}, x\Omega_{i1}, u_{i\zeta 1})$, $\mathbf{u}_{e1} = (x\varphi_{e1}, x\Omega_{e1}, u_{e\zeta 1})$ and perturbed density

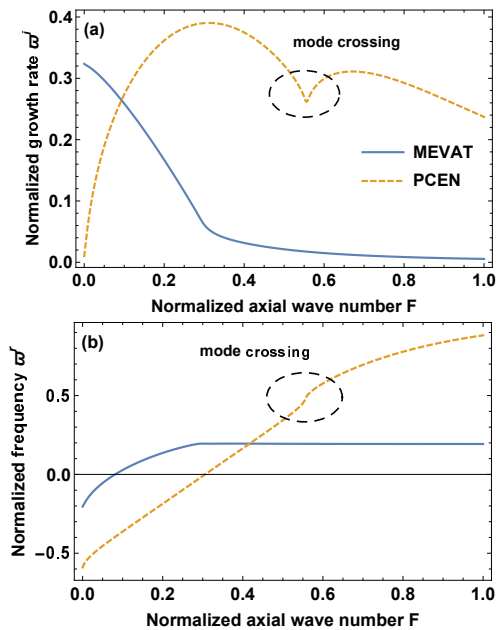


FIG. 4. Dispersion curves for MEVAT (solid line) and PCEN (dashed line), generated based on the conditions shown in Table I: (a) normalized growth rate ϖ^i ; (b) normalized frequency ϖ^r . (vs normalized axial wavenumber $F = k_\zeta/\sqrt{\delta}$).

n_{i1} from the solution of $g_1(y)$ and following equations:¹⁸

$$l_{i1}(y) = \frac{-g_1(y)}{\left(1 + \frac{i}{\Psi} \left(\frac{m\Omega_{i0}^2 + 2m\Psi - \varpi}{f(y) - 2im} \right)\right)}, \quad (13)$$

$$\chi_1(y) = -\frac{\lambda}{Z} l_{i1}(y) - \left(1 + \frac{\lambda}{Z}\right) g_1(y), \quad (14)$$

$$\begin{aligned} \varphi_{i1}(y) = & \frac{2\varpi}{i(\varpi^2 - C^2) - \varpi\delta\xi_\perp e^{-y}} [\Psi(l'_{i1}(y) - X'_1(y)) \\ & - \frac{m\Psi C}{2\varpi y} l_{i1}(y) - \left(\frac{iC}{2\varpi} + \frac{\delta\xi_\perp e^{-y}}{2}\right) \varphi_{e1}(y)], \end{aligned} \quad (15)$$

$$\begin{aligned} \varphi_{e1}(y) = & \frac{2\varpi}{\varpi + i\delta\xi_\perp e^{-y}} \left[\frac{im\Psi}{2y} X_1(y) - \Psi\delta\xi_\perp e^{-y} X'_1(y) \right. \\ & + \delta\xi_\perp e^{-y} \left(-\frac{m\Psi}{2\varpi y} + \frac{\Omega_{i0}^2}{2} + \Psi \right) l_{i1}(y) \\ & \left. + \frac{iC\delta\xi_\perp e^{-y}}{2\varpi} \varphi_{i1}(y) \right], \end{aligned} \quad (16)$$

$$\Omega_{i1}(y) = \frac{1}{\varpi} \left[m\Psi \frac{l_{i1}(y)}{y} + i(\varphi_{e1}(y) - C\varphi_{i1}(y)) \right], \quad (17)$$

$$u_{iz1}(y) = \frac{\sqrt{\delta} F \Psi}{\varpi} l_{i1}(y). \quad (18)$$

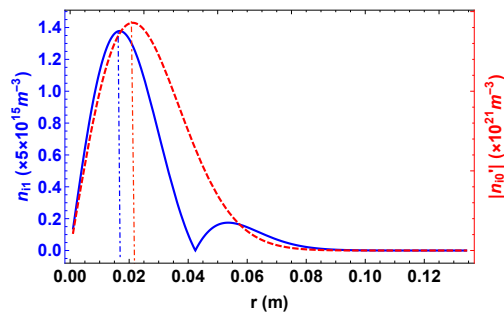


FIG. 5. Radial variations of perturbed density $n_{i1}(r)$ (solid) and equilibrium density gradient $|n'_{i0}(r)|$ (dashed line).

Figure 5 displays the radial profiles of perturbed density $n_{i1}(r)$ and equilibrium density gradient $|n'_{i0}(r)|$. We can see that the perturbed density peaks ($6.89 \times 10^{15} \text{ m}^{-3}$) at $r = 1.68 \text{ cm}$, which is very close to the radial location $r = 2.12 \text{ cm}$ of maximum density gradient ($1.43 \times 10^{21} \text{ m}^{-3}$) in equilibrium state. This suggests that the observed instability shown in Fig. 4 may be a resistive drift mode, which is driven by plasma density gradient. Temporal evolution of the cross sectional mass flow is given in Fig. 6, for a period of $t = 1 \text{ s}$. The time dependence was achieved by multiplying $\exp[i(2\pi t)]$ with $m_i(n_{i1}\mathbf{u}_{i0} + n_{i0}\mathbf{u}_{i1})$. Here, the external magnetic field and z point into the page, and coordinates x and y label the cross section of plasma column, namely $x = r \cos \theta$ and $y = r \sin \theta$. We can see that there exists a radial layer inside which the mass flow rotates in the anti-clockwise direction (same to the direction of ion diamagnetic drift), while it rotates in the clockwise direction (same to the direction of electron diamagnetic drift) outside, indicating a circularly sheared flow near the layer. The radial location of this layer is around the mode transition radius of $r = 4.24 \text{ cm}$ shown in Fig. 5, from $n = 0$ mode to $n = 1$ mode. This new pattern of rotation is different from the symmetric rotation observed before,¹⁸ and may be attributed to the large difference between electron and ion temperatures and very low normalized resistivity along the equilibrium magnetic field. Moreover, the mass flow is largest around the peak density gradient at $r = 2.12 \text{ cm}$, and drops to zero when approaching to the core and edge of plasma column, consistent with the boundary conditions of perturbed density (Fig. 5). Although only linear oscillatory response is considered here, the rotation may be damped by a similar nonlinear flow pattern as claimed before.¹⁸

D. Parameter dependence

To guide the experimental design of an efficient MEVAT, this section is devoted to studying the effects of rotation frequency, field strength, electron temperature and cathode material on the growth rate and frequency of plasma instability. As shown in Fig. 7, the normalized growth rate and frequency decrease when the rotation frequency is reduced (till $\Omega = 0.2$), consistent with a previous observation,¹⁸ because the centrifugal force is descending. However, when the rotation frequency drops below $\Omega = 0.1$, the instability becomes much stronger and the profile of dispersion curve changes remarkably, indicating the entrance into a different fluctuation mode. Figure 8 shows the influence of external magnetic field strength on the dispersion relation of MEVAT. Different from previous conclusion, however, the normalized growth rate increases with growing field strength, although the

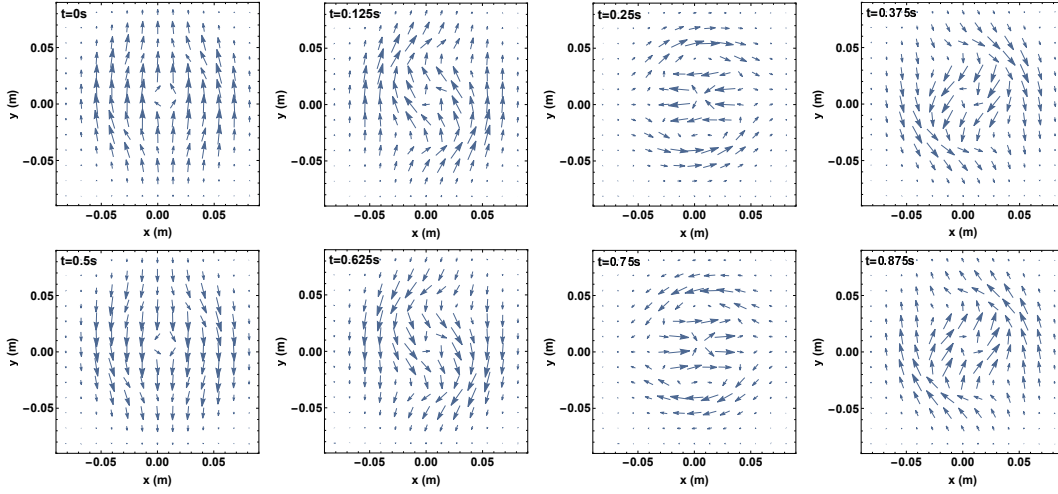


FIG. 6. Vector plots of perturbed mass flow for $m = 1$ mode in the cross section of MEVAT during one period of 1 s.

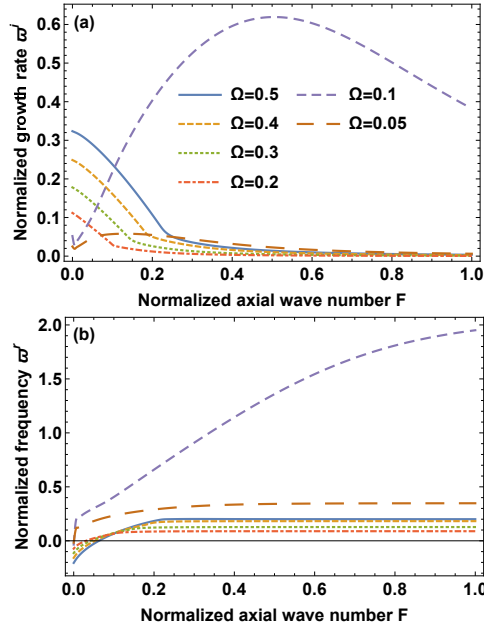


FIG. 7. Dependence of normalized growth rate ϖ^i (a) and normalized frequency ϖ^r (b) on plasma rotation frequency Ω . (vs normalized axial wavenumber $F = k_z/\sqrt{\delta}$).

normalized frequency decreases as before.¹⁸ Moreover, as shown in Fig. 9, the normalized growth rate also increases with descending electron temperature, different from previous observation, whereas the frequency drops slightly at expected.¹⁸ We claim that this unusual variation of growth rate with field strength and electron temperature may be attributed to the extremely low normalized resistivity parallel to external field, namely $\delta = 7.8 \times 10^{-5}$, which makes the plasma nearly an ideal MHD medium. Additionally, we varied the ion temperature from $T_i = 50$ eV to $T_i = 10$ eV, and found that the change in dispersion curves is

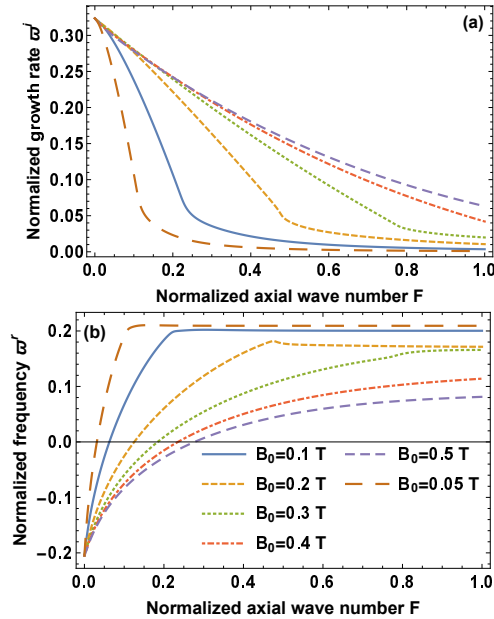


FIG. 8. Dependence of normalized growth rate ϖ^i (a) and normalized frequency ϖ^r (b) on external magnetic field strength B_0 . (vs normalized axial wavenumber $F = k_z/\sqrt{\delta}$).

even smaller and negligible. Finally, we compare the plasma instability for different cathode materials, which are commonly used in MEVAT, including Ti for previous sections, magnesium (Mg), cuprum (Cu), molybdenum (Mo) and wolfram (W). As the atomic weight is increased, the normalized growth rate drops and the normalized frequency increases slightly, which is perhaps comprehensible in the sense that ions become heavier so that move slower.

IV. CONCLUSIONS

To describe the plasma instability associated with plasma rotation and axial streaming, a two-fluid flowing plasma model developed originally for vacuum arc centrifuge is applied to MEVAT. Based on typical experimental data, the dispersion curve showing the growth rate and frequency of instability evolution is first computed via a numerical shooting method. The strongest instability occurs on axis for rotation frequency close to that of vacuum arc centrifuge, and its frequency is smaller than the sum of rotation frequency and axial velocity. Then the perturbed density is calculated through a linearized technique, which shows a radial mode transition from $n = 0$ to $n = 1$ at $r = 4.24$ m, and it peaks near the radial location of maximum equilibrium density gradient, suggesting that the observed instability is a resistive drift mode driven by density gradient. Moreover, the temporal visualization of perturbed mass flow in the cross section of plasma column shows an anti-clockwise rotation (same to the direction of ion diamagnetic drift) inside the mode transition layer, and clockwise rotation (same to the direction of electron diamagnetic drift) outside. This implies that the plasma instability is dominated by different particle species in the core (ion) and at edge (electron). Finally, parameter scan shows that the instability strength increases with growing rotation frequency and field strength, and decreases with growing

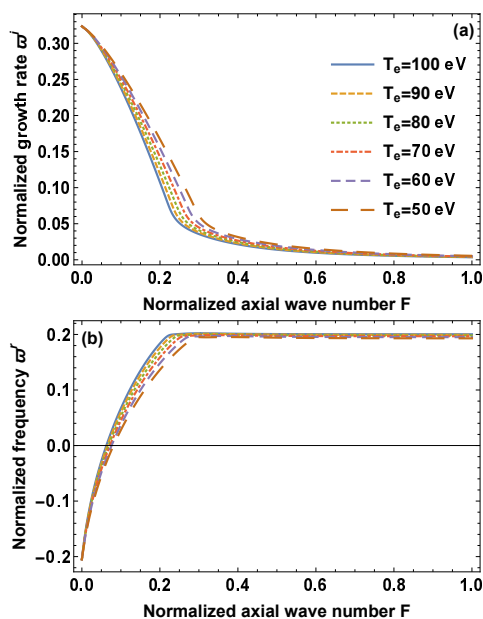


FIG. 9. Dependence of normalized growth rate ϖ^i (a) and normalized frequency ϖ^r (b) on electron temperature T_e . (vs normalized axial wavenumber $F = k_z/\sqrt{\delta}$).

electron temperature and atomic weight. Possible reasons are suggested. Further research may focus on the comparison between these computations and experimental measurements on a well diagnosed MEVAT, and extend the analysis to other plasma thrusters where instability caused by plasma rotation and axial flow is of particular concern. These relevant thrusters may include helicon double layer thruster,⁴¹ Hall thruster,⁴² magnetized ion engine,⁴³ radio-frequency plasma thruster,^{44,45} micro-wave (electron cyclotron resonance) plasma thruster,^{46,47} and variable specific impulse magnetoplasma rocket (VASIMR),⁴⁸ to name a few.

ACKNOWLEDGMENTS

This work is supported by various fundings: National Natural Science Foundation of China (11405271), China Postdoctoral Science Foundation (2017M612901), Chongqing Science and Technology Commission (cstc2017jcyjAX0047), Chongqing Postdoctoral Special Foundation (Xm2017109), Fundamental Research Funds for Central Universities (YJ201796), Pre-research of Key Laboratory Fund for Equipment (61422070306), and Laboratory of Advanced Space Propulsion (LabASP-2017-10).

REFERENCES

- ¹K. E. Clark. Survey of electric propulsion capability. *Journal of Spacecraft and Rockets*, 12(11):641, 1975.
- ²M. Martinez-Sanchez and J. E. Pollard. Spacecraft electric propulsion-an overview. *Journal of Propulsion and Power*, 14(5):688, 1998.
- ³C. Charles. Plasmas for spacecraft propulsion. *Journal of Physics D: Applied Physics*, 42(16):163001, 2009.

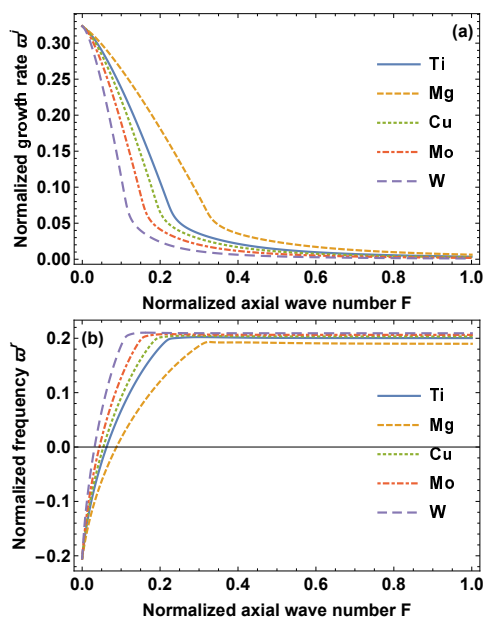


FIG. 10. Dependence of normalized growth rate ϖ^i (a) and normalized frequency ϖ^r (b) on cathode material. (vs normalized axial wavenumber $F = k_\zeta/\sqrt{\delta}$).

- ⁴D. Rafalskyi and A. Aanesland. Brief review on plasma propulsion with neutralizer-free systems. *Plasma Sources Science and Technology*, 25(4):043001, 2016.
- ⁵S. Mazouffre. Electric propulsion for satellites and spacecraft: established technologies and novel approaches. *Plasma Sources Science and Technology*, 25(3):033002, 2016.
- ⁶I. Levchenko, S. Xu, G. Teel, D. Mariotti, M. L. R. Walker, and M. Keidar. Recent progress and perspectives of space electric propulsion systems based on smart nanomaterials. *Nature Communications*, 9(1):879, 2018.
- ⁷R. W. Boswell. Plasma production using a standing helicon wave. *Physics Letters A*, 33(7):457, 1970.
- ⁸F. R. Chang Daz. The vasmir engine: Concept development, recent accomplishments and future plans. *Fusion Science and Technology*, 43(1T):3, 2003.
- ⁹A. V. Arefiev and B. N. Breizman. Theoretical components of the vasmir plasma propulsion concept. *Physics of Plasmas*, 11(5):2942, 2004.
- ¹⁰C. Charles, R. W. Boswell, and M. A. Lieberman. Xenon ion beam characterization in a helicon double layer thruster. *Applied Physics Letters*, 89(26):261503, 2006.
- ¹¹C. Charles, R. W. Boswell, W. Cox, R. Laine, and P. MacLellan. Magnetic steering of a helicon double layer thruster. *Applied Physics Letters*, 93(20):201501, 2008.
- ¹²L. Lorello, I. Levchenko, K. Bazaka, M. Keidar, L. X. Xu, S. Huang, J. W. M. Lim, and S. Y. Xu. Hall thrusters with permanent magnets: Current solutions and perspectives. *IEEE Transactions on Plasma Science*, 46(2):2390, 2018.
- ¹³C. S. Corr and R. W. Boswell. Nonlinear instability dynamics in a high-density, high-beta plasma. *Physics of Plasmas*, 16(2):022308, 2009.
- ¹⁴T. Zhuang, A. Shashurin, and M. Keidar. Plasma rotation in a micro-vacuum arc thruster. In *2010 IEEE 37th International Conference on Plasma Sciences*, Norfolk, VA, USA, 20-24 June 2010.
- ¹⁵A. Fruchtman, R. Gueroult, and N. J. Fisch. Rigid-body rotation of an electron cloud in divergent magnetic fields. *Physics of Plasmas*, 20(7):073502, 2013.
- ¹⁶E. M. Aguirre, E. E. Scime, D. S. Thompson, and T. N. Good. Spatial structure of ion beams in an expanding plasma. *Physics of Plasmas*, 24(12):123510, 2017.
- ¹⁷J. Schein and M. Keidar. Modeling of a magnetically enhanced vacuum arc thruster. In *40th AIAA/ASME/SAE/ASEE Joint Propulsion Conference and Exhibit*, number 4117, 11-14 July 2004.
- ¹⁸L. Chang, M. J. Hole, and C. S. Corr. A flowing plasma model to describe drift waves in a cylindrical helicon discharge. *Physics of Plasmas*, 18(4):042106, 2011.

- ¹⁹M. Li, H. B. Tang, J. X. Ren, and T. M. York. Modeling of plasma processes in the slowly diverging magnetic fields at the exit of an applied-field magnetoplasmadynamic thruster. *Physics of Plasmas*, 20(10):103502, 2013.
- ²⁰K. F. Lskow, P. R. C. Neumann, G. Bandelow, J. Duras, D. Kahnfeld, S. Kemnitz, P. Matthias, K. Matyash, and R. Schneider. Particle-in-cell simulation of the cathodic arc thruster. *Physics of Plasmas*, 25(1):013508, 2018.
- ²¹O. O. Baranov, U. Cvelbar, and K. Bazaka. Concept of a magnetically enhanced vacuum arc thruster with controlled distribution of ion flux. *IEEE Transactions on Plasma Science*, 46(2):304, February 2018.
- ²²E. Y. Choueiri. Plasma oscillations in hall thrusters. *Physics of Plasmas*, 8(4):1411–1426, 2001.
- ²³T. Lafleur, S. D. Baalrud, and P. Chabert. Characteristics and transport effects of the electron drift instability in hall-effect thrusters. *Plasma Sources Science and Technology*, 26(2):024008, 2017.
- ²⁴A. S. Gilmour. In *AIAA 5th Electric Propulsion Conference*, pages 66–202, San Diego, CA, USA, March 1966.
- ²⁵A. S. Gilmour, R. J. Clark, and H. Veron. In *AIAA Electric Propulsion and Plasmadynamics Conference*, pages 67–737, Colorado Springs, CO, USA, September 1967.
- ²⁶A. Anders, S. Anders, and I. G. Brown. Transport of vacuum arc plasmas through magnetic macroparticle filters. *Plasma Sources Science and Technology*, 4(1):1, 1995.
- ²⁷M. Keidar, I. Beilis, R. L. Boxman, and S. Goldsmith. 2d expansion of the low-density interelectrode vacuum arc plasma jet in an axial magnetic field. *Journal of Physics D: Applied Physics*, 29(7):1973, 1996.
- ²⁸M. Keidar, J. Schein, K. Wilson, A. Gerhan, M. Au, B. Tang, L. Idzkowski, M. Krishnan, and I. I. Beilis. Magnetically enhanced vacuum arc thruster. *Plasma Sources Science and Technology*, 14(4):661, 2005.
- ²⁹M. J. Hole, R. S. Dallaqua, S. W. Simpson, and E. Del Bosco. Plasma instability of a vacuum arc centrifuge. *Physical Review E*, 65:046409, 2002.
- ³⁰L. Spitzer. *Physic of Fully Ionized Gases*. John Wiley and Sons, 1962.
- ³¹R. S. Dallaqua, E. Del Bosco, R. P. da Silva, and S. W. Simpson. Langmuir probe measurements in a vacuum arc plasma centrifuge. *IEEE Transactions on Plasma Science*, 26(3):1044, 1998.
- ³²M. Keidar, T. Zhuang, A. Shashurin, G. Teel, D. Chiu, J. Lukas, S. Haque, and L. Brieda. Electric propulsion for small satellites. *Plasma Physics and Controlled Fusion*, 57(1):014005, 2014.
- ³³E. A. Zverev and I. A. Krinberg. Heating of a current filament and formation of constrictions in a pulsed vacuum discharge. *Technical Physics Letters*, 24(9):728, 1998.
- ³⁴J. Kutzner and H. C. Miller. Integrated ion flux emitted from the cathode spot region of a diffuse vacuum arc. *Journal of Physics D: Applied Physics*, 25(4):686, 1992.
- ³⁵R. Dethlefsen. Performance measurements on a pulsed vacuum arc thruster. *AIAA Journal*, 6(6):1197, 1968.
- ³⁶N. Qi, J. Schein, R. Binder, M. Krishnan, A. Anders, and J. Polk. In *37th Joint Propulsion Conference*, number AIAA-2001-3793, Salt Lake City, UT, USA, 8-11 July 2001.
- ³⁷J. Schein, N. Qi, R. Binder, M. Krishnan, J. K. Ziemer, J. E. Polk, and A. Anders. Inductive energy storage driven vacuum arc thruster. *Review of Scientific Instruments*, 73(2):925–927, 2002.
- ³⁸J. Schein, M. Krishnan, J. Ziemer, and J. Polk. In *Nanotech Conference*, number AIAA-2002-5716, 2002.
- ³⁹J. Schein, A. Gerhan, F. Rysanek, and M. Krishnan. Vacuum arc thruster for cubesat propulsion. In *28th IEPC*, number IEPC-0276, 2003.
- ⁴⁰R. R. Prasad and M. Krishnan. Theoretical and experimental study of rotation in a vacuum?arc centrifuge. *Journal of Applied Physics*, 61(1):113, 1987.
- ⁴¹C. Charles. Effects of cross field diffusion in a low pressure high density oxygen/silane plasma. *Journal of Vacuum Science and Technology A*, 20(4):1275–1283, 2002.
- ⁴²D. R. Yu, C. S. Wang, L Q. Wei, C. Gao, and G. Yu. Stabilizing of low frequency oscillation in hall thrusters. *Physics of Plasmas*, 15(11):113503, 2008.
- ⁴³J. R. Brophy. Nasa?s deep space 1 ion engine. *Review of Scientific Instruments*, 73(2):1071–1078, 2002.
- ⁴⁴T. A. Lafleur. *Helicon Wave Propagation in Low Diverging Magnetic Fields*. PhD thesis, The Australian National University, 2011.
- ⁴⁵A. Shabshelowitz and A. D. Gallimore. Performance and probe measurements of a radio-frequency plasma thruster. *Journal of Propulsion and Power*, 29(4):919, 2013.
- ⁴⁶B. W. Stallard, E. B. Hooper, and J. L. Power. Whistler-driven, electron-cyclotron-resonance-heated thruster: experimental status. *Journal of Propulsion and Power*, 12(4):814, 1996.
- ⁴⁷H. Kuninaka and S. Satori. Development and demonstration of a cathodeless electron cyclotron resonance ion thruster. *Journal of Propulsion and Power*, 14(6):1022, 1998.
- ⁴⁸F. F. Chang-Diaz. *Science of America*, 283(90), 2000.

